

LIMOncello: Iterated Error-State Kalman Filter on the SGal(3) Manifold for Fast LiDAR–Inertial Odometry

Carlos Pérez-Ruiz, Joan Solà

Abstract—This work introduces *LIMOncello*, a tightly coupled LiDAR–Inertial Odometry system that models 6-DoF motion on the SGal(3) manifold within an Iterated Error-State Kalman Filter backend. Compared to state representations defined on $SO(3) \times \mathbb{R}^6$, the use of SGal(3) provides a coherent and numerically stable discrete-time propagation model that helps limit drift in low-observability conditions.

LIMOncello also includes a lightweight incremental i-Octree mapping backend that enables faster updates and substantially lower memory usage than incremental kd-tree style map structures, without relying on locality-restricted search heuristics. Experiments on multiple real-world datasets show that LIMOncello achieves competitive accuracy while improving robustness in geometrically sparse environments. The system maintains real-time performance with stable memory growth and is released as an extensible open-source implementation at <https://github.com/CPerezRuiz335/LIMOncello>.

Index Terms—SLAM, LiDAR-inertial odometry, SGal(3) manifold, i-Octree mapping

I. INTRODUCTION

Simultaneous Localization and Mapping (SLAM) is essential for mobile robotics, as it provides the accurate ego-motion and the consistent map required for safe planning, control, and higher-level perception. Historically, vision-based systems have been widely used, but their robustness is highly compromised on ambient illumination, texture-less scenes, and often indirect depth estimation.

Light detection and ranging (LiDAR) sensors complement vision in such setups by providing long-range, illumination-invariant, and metrically accurate depth, which translates into reliable odometry and mapping across diverse environments. However, LiDAR introduces distinct challenges: *i*) processing a massive, continuous stream of data in a timely and efficient manner, *ii*) overcome the scarcity of reliable geometric features in structurally poor environments, and *iii*) correcting the scan deformation caused by sensor movement during data capture [1], [2].

To address these issues, LiDAR–Inertial Odometry (LIO) combines LiDAR with high-rate inertial measurements. High-rate Inertial Measurement Unit (IMU) measurements enable per-point deskewing and cover the latency between LiDAR frames, while LiDAR provides metric structure to correct the robot’s pose. Most LIO systems are organized into a front-end and a back-end [3]. The front-end maintains a history map and performs fast data association. This process is based on classical point-cloud registration, which works by finding the nearest neighbors for each incoming point. These neighbors

are then used to fit a simple local model (typically a plane or a line) and form the residuals for optimization.

The back-end is responsible for state optimization, with the two common families being graph-based smoothing and filtering. Under limited onboard processing, filtering based on the Extended Kalman Filter and its iterated error-state (IESKF) variant is often preferred [4], as exemplified by FAST-LIO1 [1] and FAST-LIO2 works [2].

A key step forward was the IKFoM [4] framework, which formalized the IESKF on differentiable manifolds and packaged it into a practical toolkit. This gave a canonical discrete-time representation and clean separation between manifold operations and system-specific models.

With a robust and reusable back-end in place, the community has focused effort on the front-end problems of features and computation: designing faster spatial data structures and residual evaluations that sustain real-time rates without sacrificing accuracy. The community has improved classical k-d tree map structures with incremental variants such as the ikd-Tree [5] and sparse voxel representations like iVox [3], enabling efficient real-time updates and queries. Building on these advances, recent methods have shifted from point-to-map registration to point-to-feature formulations, where points are aligned with local geometric primitives (*e.g.*, planes or edges) rather than individual map points [6], [7].

Alongside discrete-time pipelines, continuous-time motion models have gained attraction. By representing the trajectory with piecewise functions and evaluating residuals at each point timestamp, these methods improve deskewing and alignment during fast motion or asynchronous sensing. Recent systems such as DLIO [8] adopt point-wise continuous-time motion compensation, and others like RESPLE [9] show that investing in state representation and motion modeling can yield competitive accuracy while preserving real-time performance.

Most LIO frameworks rely on what is often referred to as a *compound* [4] or *bundle manifold* [10] representation of the state. In these formulations, the system’s pose, and velocity are defined on separate sub-manifolds—usually $SO(3) \times \mathbb{R}^6$. While this decomposition simplifies the implementation, it also neglects certain kinematic couplings between translational and rotational motion, leading to an approximation that may lose accuracy under highly dynamic motion or under sustained low-observability conditions, *e.g.*, near-zero acceleration that reduces IMU observability, or degenerate LiDAR environments such as long corridors.

Beyond Euclidean and compound representations, several Lie-group manifolds have been adopted in robotics. $SE(3)$ is widely used for pose estimation, while $SE_2(3)$ became standard in Invariant EKF-based methods [11], with extensions

All authors are with Mobile Robotics Laboratory, Institut de Robòtica i Informàtica Industrial, Universitat Politècnica de Catalunya, Barcelona, Spain {cperez, jsola}@iri.upc.edu

such as $SE_N(3)$ [12] and $SGal(3)$ explored more recently in equivariant filtering [13]. However, their use in tightly coupled LIO-SLAM systems remains limited.

In this direction, this letter presents **LIMOncello** (**Localize Intensively, Map Online**), the first LIO-SLAM system built upon the $SGal(3)$ manifold within the IKFoM framework. To the best of our knowledge, this is the first attempt to evaluate the suitability of $SGal(3)$ for tightly-coupled LIO systems.

The main contributions of this work are summarized as follows:

- **Novel state representation:** We integrate the $SGal(3)$ manifold into IKFoM’s IESKF framework, enabling consistent 6-DoF motion estimation and improved robustness under low LiDAR observability.
- **Efficient spatial data structure:** We replace the widely used ikd-Tree with a refactored, lightweight i-Octree implementation [14], achieving faster incremental updates and lower computational overhead by avoiding costly tree rebalancing.
- **Modular and extensible implementation:** LIMOncello is implemented using the `manif` library [15], resulting in a clean, modular codebase that is easily extensible and publicly available.

II. PRELIMINARIES

A. Differentiable manifolds

Informally, a *manifold* \mathcal{M} of dimension m is a set which is locally homeomorphic to \mathbb{R}^m : for every element $\mathcal{X} \in \mathcal{M}$ there exists a local neighbourhood that can be smoothly mapped to \mathbb{R}^m . For a differentiable manifold, such space always exists and is chosen as the tangent space at \mathcal{X} , *i.e.*, $T_{\mathcal{X}}\mathcal{M}$.

When the manifold \mathcal{M} is also a *Lie group*, the tangent space at the identity, $T_{\mathcal{E}}\mathcal{M}$, is provided with a multiplication operation—typically non-associative—called the *Lie bracket*, which gives $T_{\mathcal{E}}\mathcal{M}$ an additional algebraic structure known as the *Lie algebra*, denoted \mathfrak{m} . This structure encapsulates the structure of the manifold. The elements of the tangent space can be interpreted as velocities or time derivatives, as well as error and increment variables used in estimation and control, for elements evolving on \mathcal{M} [10].

Lie groups are naturally endowed with the exponential and logarithmic mappings, \exp and \log , which provide smooth isomorphisms between the manifold and its Lie algebra. The elements τ^\wedge of the Lie algebra have non-trivial structures (*e.g.*, skew-symmetric matrices or imaginary numbers), yet they can always be written as linear combinations of the algebra’s *generators* through the *wedge* $(\cdot)^\wedge$ and *vee* $(\cdot)^\vee$ operators, which provide convenient mapping to \mathbb{R}^m , where computations can be performed in a standard vector space while preserving the group’s geometry.

We now introduce the operators \oplus and \ominus , which enable the combination of linear increments, expressed in the tangent vector space, with elements of the manifold. Following the convention in [10], increments expressed in the local frame

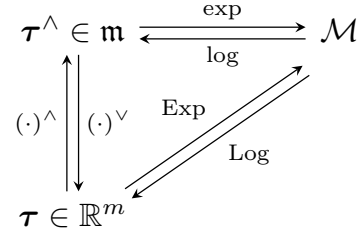


Fig. 1. Commutative diagram of the mappings between \mathbb{R}^m , the Lie algebra \mathfrak{m} , and the manifold \mathcal{M} , including the shortcuts $\text{Exp} = \exp(\tau^\wedge)$ and $\text{Log} = \log(\mathcal{X})^\vee$.

(*e.g.*, IMU readings) are always placed on the right-hand side of the composition,

$$\oplus : \mathcal{Y} = \mathcal{X} \oplus \tau \triangleq \mathcal{X} \circ \text{Exp}(\tau) \in \mathcal{M}, \quad (1a)$$

$$\ominus : \tau = \mathcal{Y} \ominus \mathcal{X} \triangleq \text{Log}(\mathcal{X}^{-1} \circ \mathcal{Y}) \in T_{\mathcal{X}}\mathcal{M}, \quad (1b)$$

where \circ is the composition operation between elements of the group. In this letter we stick to Lie Groups that belong to $GL(n)$ —the space of all invertible square matrices—and the trivial Euclidean space \mathbb{R}^n . Then, \circ reduces to matrix multiplication, or to vector addition, respectively, while \exp becomes the matrix exponential for matrix Lie groups.

However, when the manifold is not a Lie group, the \exp and \log maps are not formally defined. In such cases, the operators \oplus and \ominus are usually called retraction and lift, respectively. Although their specific implementation depends on the manifold under consideration, we retain the same notation to express how a tangent perturbation modifies an on-manifold element.

For a more exhaustive introduction to Lie theory, we refer the reader to [10].

B. IESKF on Manifolds

In the IESKF—and ESKF—formulation, the true-state is expressed as a suitable composition (*e.g.*, linear sum, matrix product) of the nominal- and the error-state. The idea is to consider the nominal-state integrable in a non-linear fashion, and the error-state as linearly integrable and suitable for linear-Gaussian filtering [16]. Ultimately, the goal is to determine the linearized dynamics of the error-state.

The discrete dynamics of a system require a manifold \mathcal{M} on which the state evolves, together with an operation that describes how the state is driven by a constant increment over a time interval Δt , assuming a zero-order hold discretization.

For Lie groups, this operation naturally corresponds to the \oplus operator, since group composition directly describes how an increment in the tangent space updates the state on the manifold. For example, for $\mathbf{R} \in SO(3)$ and a constant angular velocity ω over Δt , expressed in the body frame, the update is $\mathbf{R}_{k+1} = \mathbf{R}_k \oplus (\omega \Delta t)$.

When the manifold \mathcal{M} is not a Lie group, the increment does not necessarily lie in its tangent space. Hence, we adopt

the operator¹

$$\boxplus : \mathcal{M} \times \mathbb{R}^l \rightarrow \mathcal{M} \quad (2)$$

to describe the state evolution.

a) *S² manifold*: In this work, the gravity vector is represented on the 2-sphere manifold $S^2(r) \triangleq \{\mathbf{x} \in \mathbb{R}^3 : \|\mathbf{x}\| = r, r > 0\}$, following the parameterization in [4]. The S^2 manifold defines a smooth surface embedded in \mathbb{R}^3 with constant norm r , enforcing a constant-norm directional constraint.

When \mathbf{x} is represented in a fixed world frame, its state remains constant, $\dot{\mathbf{x}} = \mathbf{0}$, whereas in a rotating body frame it evolves according to $\dot{\mathbf{x}} = -\boldsymbol{\omega} \times \mathbf{x}$, where $\boldsymbol{\omega}$ is a constant angular velocity expressed in body frame. Assuming a zero-order hold discretization, the discrete update in body frame becomes

$$\mathbf{x}_{k+1} = \text{SO}(3)\text{Exp}(\boldsymbol{\omega} \Delta t)^\top \mathbf{x}_k \triangleq \mathbf{x}_{k+1} = \mathbf{x}_k \boxplus (\boldsymbol{\omega} \Delta t). \quad (3)$$

The definitions of the \oplus and \ominus operators for S^2 are provided in Appendix A.

b) *Error-state linearization*: The nominal-state \mathbf{x} does not take into account the noise terms \mathbf{w} in its dynamics, and other possible model nuances. As a consequence \mathbf{x} accumulates error, which is collected in the error-state $\delta\mathbf{x}$, and estimated through the IESKF [16]. The true-state is defined as

$$\mathbf{x}^* = \mathbf{x} \oplus \delta\mathbf{x}, \quad (4)$$

and its dynamics are

$$\mathbf{x}^* \leftarrow \mathbf{x}^* \boxplus \mathbf{f}(\mathbf{x}^*, \mathbf{u}, \mathbf{w}), \quad (5)$$

where $x \leftarrow f(x, \bullet)$ stands for a time update of the type $x_{k+1} = f(x_k, \bullet_k)$, \mathbf{f} is the function that creates a suitable increment over Δt and \mathbf{u} is the control signal.

Substituting (4) into (5), the time evolution of the error state is defined as

$$\begin{aligned} \delta\mathbf{x}_{k+1} &= \mathbf{x}_{k+1}^* \ominus \mathbf{x}_{k+1} \\ &\leftarrow (\mathbf{x}^* \boxplus \mathbf{f}(\mathbf{x}^*, \mathbf{u}, \mathbf{w})) \ominus (\mathbf{x} \boxplus \mathbf{f}(\mathbf{x}, \mathbf{u}, \mathbf{0})) \\ &\leftarrow \underbrace{((\mathbf{x} \oplus \delta\mathbf{x}) \boxplus \mathbf{f}(\mathbf{x} \oplus \delta\mathbf{x}, \mathbf{u}, \mathbf{w}))}_{\text{A}} \ominus \underbrace{(\mathbf{x} \boxplus \mathbf{f}(\mathbf{x}, \mathbf{u}, \mathbf{0}))}_{\text{B}} \end{aligned} \quad (6)$$

In the IESKF prediction, the error-state is linearized as $\delta\mathbf{x}_{k+1} \simeq \mathbf{F}_{\delta\mathbf{x}} \delta\mathbf{x} + \mathbf{F}_{\mathbf{w}} \mathbf{w}$, where

$$\mathbf{F}_{\delta\mathbf{x}} = \left. \frac{\partial \delta\mathbf{x}_{k+1}}{\partial \delta\mathbf{x}_k} \right|_{\delta\mathbf{x}=\mathbf{0}, \mathbf{w}=\mathbf{0}}, \quad (7a)$$

$$\mathbf{F}_{\mathbf{w}} = \left. \frac{\partial \delta\mathbf{x}_{k+1}}{\partial \mathbf{w}} \right|_{\delta\mathbf{x}=\mathbf{0}, \mathbf{w}=\mathbf{0}}, \quad (7b)$$

and these Jacobians can be computed by the chain rule as

$$\mathbf{F}_{\delta\mathbf{x}} = \frac{\partial \text{A} \ominus \text{B}}{\partial \text{A}} \left(\frac{\partial \text{A}}{\partial (\mathbf{x} \oplus \delta\mathbf{x})} + \frac{\partial \text{A}}{\partial \mathbf{f}(\bullet)} \frac{\partial \mathbf{f}(\bullet)}{\partial (\mathbf{x} \oplus \delta\mathbf{x})} \right) \frac{\partial (\mathbf{x} \oplus \delta\mathbf{x})}{\partial \delta\mathbf{x}}, \quad (8a)$$

$$\mathbf{F}_{\mathbf{w}} = \frac{\partial \text{A} \ominus \text{B}}{\partial \text{A}} \frac{\partial \text{A}}{\partial \mathbf{f}(\bullet)} \frac{\partial \mathbf{f}(\bullet)}{\partial \mathbf{w}}. \quad (8b)$$

¹The \oplus - \ominus and \boxplus notations are flipped *w.r.t.* IKFoM to be consistent with the notation in Solà et al. [10].

Note that when \mathbf{x} lives in a Lie group,

$$\mathbf{F}_{\delta\mathbf{x}} = \mathbf{Ad}_{\text{Exp}(\mathbf{f}(\bullet))}^{-1} + \mathbf{J}_r(\mathbf{f}(\bullet)) \frac{\partial \mathbf{f}(\mathbf{x} \oplus \delta\mathbf{x}, \mathbf{u}, \mathbf{w})}{\partial (\mathbf{x} \oplus \delta\mathbf{x})}, \quad (9a)$$

$$\mathbf{F}_{\mathbf{w}} = \mathbf{J}_r(\mathbf{f}(\bullet)) \frac{\partial \mathbf{f}(\mathbf{x} \oplus \delta\mathbf{x}, \mathbf{u}, \mathbf{w})}{\partial \mathbf{w}}, \quad (9b)$$

where \mathbf{Ad} is the Adjoint map [10, eq. (30)], and \mathbf{J}_r the right Jacobian [10, eq. (67)].

C. SGal(3)

The Special Galilean group SGal(3) provides a natural framework for the propagation of motion estimates over time, particularly in situations where temporal uncertainty plays a significant role [17]. By representing the state as a Galilean frame, time is intrinsically incorporated into the group structure, allowing spatial and temporal quantities to evolve jointly. This coupling captures the fundamental relationship between uncertainty in space and uncertainty in time, since uncertainty about *when* directly translates into uncertainty about *where* [18].

First used in robotics in [19] under the name of *IMU deltas matrix Lie group*, SGal(3) is a 10-dimensional Lie group that can be interpreted as the group of transformations that move points in both space and time—unlike SE(3) that only represents rigid motions in 3D space.

Elements of SGal(3) can be written as 5×5 matrices,

$$\Gamma = \begin{bmatrix} \mathbf{R} & \mathbf{v} & \mathbf{p} \\ \mathbf{0} & 1 & t \\ \mathbf{0} & \mathbf{0} & 1 \end{bmatrix} \in \text{SGal}(3) \subset \mathbb{R}^{5 \times 5}, \quad (10)$$

where $\mathbf{R} \in \text{SO}(3)$ is the rotation, $\mathbf{v} \in \mathbb{R}^3$ is the linear velocity, $\mathbf{p} \in \mathbb{R}^3$ is the position, and $t \in \mathbb{R}$ is the time variable. Its Lie algebra $\mathfrak{sgal}(3)$ is also written as a 5×5 matrix

$$\tau^\wedge = \begin{bmatrix} [\boldsymbol{\theta}]_\times & \boldsymbol{\nu} & \boldsymbol{\rho} \\ \mathbf{0} & 1 & \iota \\ \mathbf{0} & \mathbf{0} & 1 \end{bmatrix} \in \mathfrak{sgal}(3), \quad \tau = \begin{bmatrix} \boldsymbol{\rho} \\ \boldsymbol{\nu} \\ \boldsymbol{\theta} \\ \iota \end{bmatrix}, \quad (11)$$

where $[\boldsymbol{\theta}]_\times \in \mathfrak{so}(3)$ is the skew-symmetric matrix of $\boldsymbol{\theta} \in \mathbb{R}^3$, $\boldsymbol{\nu} \in \mathbb{R}^3$, $\boldsymbol{\rho} \in \mathbb{R}^3$, and $\iota \in \mathbb{R}$.

Using SGal(3), IMU propagation can be elegantly² formulated as

$$\Gamma \leftarrow \Gamma \oplus \begin{bmatrix} \mathbf{0} \\ \mathbf{a} \\ \boldsymbol{\omega} \\ 1 \end{bmatrix} \Delta t, \quad (12)$$

assuming inputs are constant during one sampling period Δt , where $\boldsymbol{\omega}$ and \mathbf{a} are the angular rates and linear accelerations, respectively.

For the definition and derivation of the exp and log maps associated with SGal(3), we refer the reader to [20].

²By comparison, IMU propagation on $\Xi \in \text{SE}_2(3)$ is often expressed as $\Xi \leftarrow \Xi \oplus \Phi(\Xi) \Delta t$, with $\Phi(\cdot)$ being an auxiliary mapping inherent to the SE₂(3) formulation, thus making the update less compact.

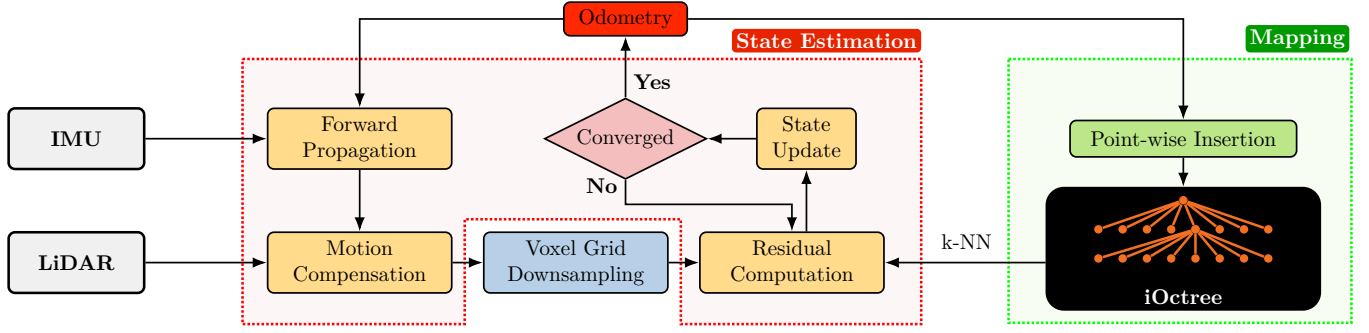


Fig. 2. **System overview.** Unlike most LIO systems, motion compensation is done first, allowing the whole point cloud to be later used for fine-grained perception on a global map as detailed as possible.

III. METHODOLOGY

A. System Overview

The overall pipeline is illustrated in Fig. 2. Incoming LiDAR scans are first deskewed using the IMU-integrated states, following the per-point deskewing strategy of [2], but with the motion model formulated on SGal(3) rather than on $SO(3) \times \mathbb{R}^6$. Between LiDAR messages, raw IMU data is continuously propagated and a window of intermediate poses is stored so that each LiDAR point can be associated with its corresponding pose during deskewing.

The downsampled point cloud is then registered against the global map to extract geometric correspondences, which are used to compute residuals for the iterated state update. Once the optimization converges, the current LiDAR frame is inserted into the global map, which is maintained as an incremental i-Octree.

B. Notation

Let the point cloud for a single LiDAR message initiated at time t_k be denoted as \mathcal{P}_k and indexed by k . The point cloud \mathcal{P}_k is composed of points $\mathbf{p}_i \in \mathbb{R}^3$ indexed by $i = 1, \dots, N$, where N is the total number of points in the scan.

The world frame is denoted as \mathcal{W} , the robot frame as \mathcal{R} (which coincides with the IMU frame I), and the LiDAR frame as \mathcal{L} . The robot's state vector \mathbf{x} is defined as the *bundle manifold*

$$\mathbf{x} = (\mathcal{W}\mathbf{T}, {}^I\mathbf{T}_L, \mathcal{R}\mathbf{b}_\omega, \mathcal{R}\mathbf{b}_a, \mathcal{W}\mathbf{g}) \in \mathcal{M}, \quad (13)$$

$$\mathcal{M} = \text{SGal}(3) \times \text{SE}(3) \times \mathbb{R}^6 \times S^2,$$

where ${}^I\mathbf{T}_L$ are the LiDAR-IMU extrinsics, $\mathcal{R}\mathbf{b}_\omega$ and $\mathcal{R}\mathbf{b}_a$ are the gyroscope and accelerometer biases, respectively, and $\mathcal{W}\mathbf{g}$ is the gravity vector. With slight abuse of notation, frame superscripts and time indices are omitted when unambiguous; variables are assumed to be at time k unless stated otherwise.

IMU measurements $\mathbf{u} = [\mathbf{a}, \boldsymbol{\omega}]$ are modeled as

$$\boldsymbol{\omega} = \boldsymbol{\omega}^* + \mathbf{b}_\omega + \mathbf{n}_\omega, \quad (14a)$$

$$\mathbf{a} = \mathbf{a}^* + \mathbf{b}_a + \mathbf{n}_a - \mathbf{R}^\top \mathbf{g}, \quad (14b)$$

where $\boldsymbol{\omega}^*$ and \mathbf{a}^* are the true angular velocity and linear acceleration. The terms \mathbf{n}_ω and \mathbf{n}_a are white measurement noise, and \mathbf{R} is the system attitude.

Biases follow a random-walk model driven by Gaussian noises \mathbf{n}_{b_ω} and \mathbf{n}_{b_a} , *i.e.*, $\dot{\mathbf{b}}_\omega = \mathbf{n}_{b_\omega}$ and $\dot{\mathbf{b}}_a = \mathbf{n}_{b_a}$. All noise terms together define

$$\mathbf{w} = [\mathbf{n}_\omega, \mathbf{n}_a, \mathbf{n}_{b_\omega}, \mathbf{n}_{b_a}].$$

C. Prediction

Based on the \boxplus operation defined in (2), and the transition matrices in (7), the discrete propagation of the nominal state and its covariance are

$$\hat{\mathbf{x}} \leftarrow \hat{\mathbf{x}} \boxplus \mathbf{f}(\hat{\mathbf{x}}, \mathbf{u}, \mathbf{0}), \quad (15a)$$

$$\hat{\mathbf{P}} \leftarrow \mathbf{F}_{\delta\hat{\mathbf{x}}} \hat{\mathbf{P}} \mathbf{F}_{\delta\hat{\mathbf{x}}}^\top + \mathbf{F}_w \mathbf{Q} \mathbf{F}_w^\top, \quad (15b)$$

where $\hat{\mathbf{x}}$ is the propagated state, $\hat{\mathbf{P}}$ the propagated covariance, and \mathbf{Q} is the covariance matrix of the noise \mathbf{w} (see [16, eq. (262)–(265), (271)]). Between LiDAR scans, multiple IMU measurements are integrated sequentially. At the first IMU of a given interval, $\hat{\mathbf{x}}$ is initialized with the last LiDAR-updated state estimate, $\bar{\mathbf{x}}_{k-1}$.

The function \mathbf{f} is given by

$$\mathbf{f}(\mathbf{x}, \mathbf{u}, \mathbf{w}) = \begin{bmatrix} \mathbf{0} \\ \mathbf{a} - \mathbf{b}_a - \mathbf{n}_a + \mathbf{R}^\top \mathbf{g} \\ \boldsymbol{\omega} - \mathbf{b}_\omega - \mathbf{n}_\omega \\ 1 \\ \mathbf{0} \\ \mathbf{n}_{b_\omega} \\ \mathbf{n}_{b_a} \\ \mathbf{0} \end{bmatrix} \Delta t. \quad (16)$$

D. Iterated Update

The iterations within the update step are initialized using the predicted prior, *i.e.*, $\hat{\mathbf{x}}_j = \hat{\mathbf{x}}$ for $j = 0$. At each iteration, for every downsampled point \mathbf{p}_i , we perform a k -NN search in the i-Octree map in order to fit a local plane through them, yielding the point-to-plane constraint used in [2].

The measurement function is

$$\mathbf{h}_i(\mathbf{x}) = \mathbf{u}_i^\top (\boldsymbol{\pi}(\mathbf{T}) {}^I\mathbf{T}_L \mathbf{p}_i - \mathbf{q}_i), \quad (17)$$

where \mathbf{u}_i is the normal of the plane fitted to the k -NN neighbors of \mathbf{p}_i , \mathbf{q}_i is any point on that plane, and $\boldsymbol{\pi}(\mathbf{T})$ is a smooth projection from SGal(3) to SE(3).

Jacobians of \mathbf{h}_i w.r.t. $\mathbf{\Gamma}$ and ${}^I\mathbf{T}_L$ are

$$\frac{\partial \mathbf{h}_i}{\partial \mathbf{\Gamma}} = \mathbf{u}_i^\top \begin{bmatrix} \mathbf{R} & -\mathbf{R} [{}^I\mathbf{T}_L \mathbf{p}_i]_\times & \mathbf{0} \end{bmatrix}, \quad (18a)$$

$$\frac{\partial \mathbf{h}_i}{\partial {}^I\mathbf{T}_L} = \mathbf{u}_i^\top \begin{bmatrix} {}^I\mathbf{R}_L & -{}^I\mathbf{R}_L [\mathbf{p}_i]_\times \end{bmatrix}, \quad (18b)$$

$$\frac{\partial \mathbf{h}_i}{\partial \mathbf{x}} = \begin{bmatrix} \frac{\partial \mathbf{h}_i}{\partial \mathbf{\Gamma}} & \frac{\partial \mathbf{h}_i}{\partial {}^I\mathbf{T}_L} & \mathbf{0} \end{bmatrix}. \quad (18c)$$

The propagated state $\hat{\mathbf{x}}_j$ and covariance $\hat{\mathbf{P}}$ from (15b) impose a prior Gaussian distribution for the unknown true state \mathbf{x}_j^* . More precisely, $\hat{\mathbf{P}}$ represents the covariance of the following error state

$$\delta \mathbf{x}_j = \mathbf{x}_j^* \ominus \hat{\mathbf{x}} = (\hat{\mathbf{x}}_j \oplus \delta \mathbf{x}_j) \ominus \hat{\mathbf{x}} \simeq \hat{\mathbf{x}}_j \ominus \hat{\mathbf{x}} + \mathbf{J}_j \delta \mathbf{x}_j, \quad (19)$$

where \mathbf{J}_j is the partial differentiation of $(\hat{\mathbf{x}}_j \oplus \delta \mathbf{x}_j) \ominus \hat{\mathbf{x}}$ w.r.t. $\delta \mathbf{x}_j$, evaluated at $\delta \mathbf{x}_j = \mathbf{0}$.

For a regular Lie group, \mathbf{J}_j coincides with the inverse of the right Jacobian [10, eq. (83)], and it transports the propagated covariance matrix $\hat{\mathbf{P}}$ to the tangent space at $\hat{\mathbf{x}}_j$, at each iteration.

Following the iterated update formulation in [2], we gather all residuals into \mathbf{z}_j and stack the partial derivatives of (17) into \mathbf{H}_j , then define the projected prior covariance as $\hat{\mathbf{P}}_j = (\mathbf{J}_j)^{-1} \hat{\mathbf{P}} (\mathbf{J}_j)^{-\top}$, and solve the Maximum A Posteriori (MAP) step via

$$\mathbf{K}_j = (\mathbf{H}_j^\top \mathbf{V}^{-1} \mathbf{H}_j + \mathbf{P}_j^{-1})^{-1} \mathbf{H}_j^\top \mathbf{V}^{-1}, \quad (20a)$$

$$\hat{\mathbf{x}}_{j+1} = \hat{\mathbf{x}}_j \oplus (-\mathbf{K}_j \mathbf{z}_j - (\mathbf{I} - \mathbf{K}_j \mathbf{H}_j) \mathbf{J}_j^{-1} (\hat{\mathbf{x}}_j \ominus \hat{\mathbf{x}})), \quad (20b)$$

where \mathbf{V} is the measurement covariance matrix.

The iterated update continues until convergence, $\|\hat{\mathbf{x}}_{j+1} \ominus \hat{\mathbf{x}}_j\| < \varepsilon$, or a maximum number of iterations is reached. After that the state and covariance are updated as $\bar{\mathbf{x}} = \hat{\mathbf{x}}_j$, and $\bar{\mathbf{P}} = (\mathbf{I} - \mathbf{K}_j \mathbf{H}_j) \hat{\mathbf{P}}_j$.

E. i-Octree

As in the i-Octree proposed in [14], each node can have up to eight children. This yields a shallower tree compared to a binary structure, and even in the worst-case branching factor, the effective complexity per level remains significantly lower. Moreover, children are indexed using Morton codes during subdivision, speeding up traversal and query operations.

Downsampling in the ikd-Tree is based on retaining the point closest to the voxel centroid. In contrast, downsampling in the i-Octree is performed by recursively subdividing an octant until it contains fewer than a specified number of points or until its spatial extent falls below a minimum threshold.

In our implementation, we omit the reallocation step that redistributes all points inside a leaf octant during subdivision, and box-wise deletion is not supported. Tree rebalancing, as in the original i-Octree, is also not performed, simplifying the structure while maintaining real-time performance.

IV. EVALUATION

We evaluate LIMOncello (LIMO) on several public real-world datasets, including MCD [21], GrandTour [22], R-Campus [9], and a specific use case from the City

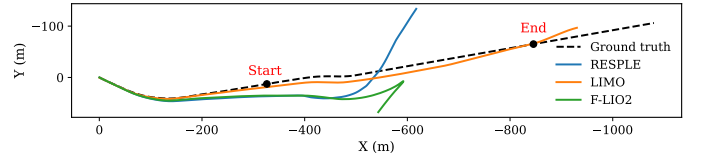
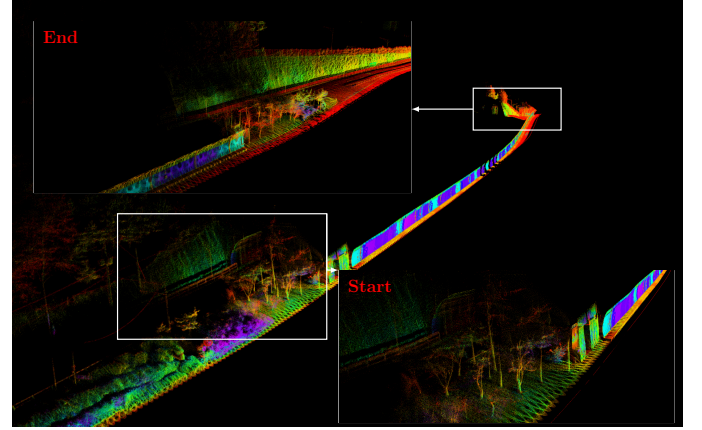


Fig. 3. Qualitative comparison of accumulated trajectories in the feature-degenerate tunnel segment of City02, using only the left-facing LiDAR. **Top:** Map reconstructed by LIMO, showing both the *start* and *end* points of the tunnel. **Bottom:** Trajectories projected onto the x-y plane and compared against ground truth during the tunnel traversal, where FAST-LIO2 exhibits an early, non-recoverable divergence. RESPLE, in contrast, continues through the tunnel but also undergoes non-recoverable drift, deviating severely from the ground truth, including descent below the ground surface. Meanwhile, LIMO is the only method that traverses the tunnel under stable conditions.

Datasets [23]. LIMO is compared against RESPLE in its LIO configuration (R-LIO) and FAST-LIO2 (F-LIO2). All experiments are executed on a laptop equipped with an Intel Ultra 5 125H CPU and 32 GB RAM.

We interpolate trajectory estimates at ground truth timestamps and compute the RMSE of the absolute position error (APE) using the *evo* library [24]. Failures are denoted by \mathbf{X} , and the best and second-best results are highlighted in **bold** and underline, respectively.

A. Datasets

1) *Grand-Tour*: We evaluate indoor and outdoor sequences, including runs with mixed stairwell passages and extended indoor-outdoor transitions. All runs use Hesai XT32 and Novatel CPT7 sensors. LIMO demonstrates robust performance under diverse conditions, without any failure, as shown in Tab. I.

TABLE I
APE (RMSE, METERS) ON GRAND-TOUR.

Method	Sequences				
	Arc_1	Con_1	Con_3	HAUS_1	Trim_1
F-LIO2	1.870	0.074	\mathbf{X}	<u>0.054</u>	<u>0.215</u>
R-LIO	0.088	<u>0.126</u>	0.041	0.040	0.037
LIMO	<u>0.371</u>	0.345	<u>0.355</u>	0.369	0.389

2) *MCD*: We use day and night sequences from the NTU Campus subset of the MCD dataset, recorded with Livox Mid70 and VN100 sensors. Tab. II shows that LIMO provides results

comparable to F-LIO2 and R-LIO, without encountering any failure.

TABLE II
APE (RMSE, METERS) ON MCD (NTU CAMPUS).

Method	Day			Night		
	01	02	10	04	08	13
F-LIO2	2.528	0.188	5.164	0.767	2.559	1.947
R-LIO	0.724	<u>0.171</u>	0.974	0.686	0.976	0.649
LIMO	<u>0.839</u>	0.156	<u>2.999</u>	0.838	<u>1.375</u>	<u>1.636</u>

3) *City Datasets*: We select a short segment from the City02 run containing a 400 m tunnel, used to evaluate the SGal(3) state representation in a highly degenerate environment. Only the left-facing Livox Avia is used in this scenario. LIMO is the only method that reaches the end of the tunnel maintaining a stable trajectory, as illustrated in Fig. 3.

4) *R-Campus*: This dataset consists of a bipedal wheeled robot equipped with a Livox Avia operating over a 1400 m campus route. The error is evaluated using the end-to-end drift between the start and end of each sequence. LIMO achieves an error of **0.22 m**, outperforming R-LIO (0.27 m) and F-LIO2 (2.70 m).

B. Tree Efficiency Analysis

We benchmark the ikd-Tree, the original i-Octree, and the proposed LIMO i-Octree under identical conditions³ on the ntu_day_01 sequence, using the OS1-128 LiDAR, and report their average processing time and memory usage.

As shown in Fig. 4, ikd-Tree exhibits substantially higher computational and memory overhead (avg. 248 ms, 10.7 GB), mainly due to its continuous rebalancing and point redistribution. In contrast, both octree variants maintain real-time performance, with average runtimes of 21.7 ms (i-Octree) and 14.6 ms (LIMO i-Octree), and stable memory footprints of approximately 100–120 MB. Our i-Octree implementation achieves the lowest runtime while retaining compact memory growth.

V. DISCUSSION

LIMOncello achieves robust and accurate LiDAR-inertial odometry across a diverse set of real-world datasets. Its SGal(3)-based state propagation captures the underlying platform kinematics, resulting in consistent motion propagation when system observability is degraded.

SGal(3) preserves the geometric coupling between translational and rotational dynamics, and this property is particularly beneficial in geometrically degenerate or feature-denied environments, where several degrees of freedom are weakly constrained by LiDAR measurements and motion propagation dominates state evolution.

The practical impact of this design choice is most evident in the City02 tunnel experiment. Due to the highly degenerate geometry and its lateral LiDAR observations, FAST-LIO2 exhibits divergence and RESPLE experiences severe

³Both octree structures use identical parameter settings. ikd-Tree is evaluated with its default configuration.

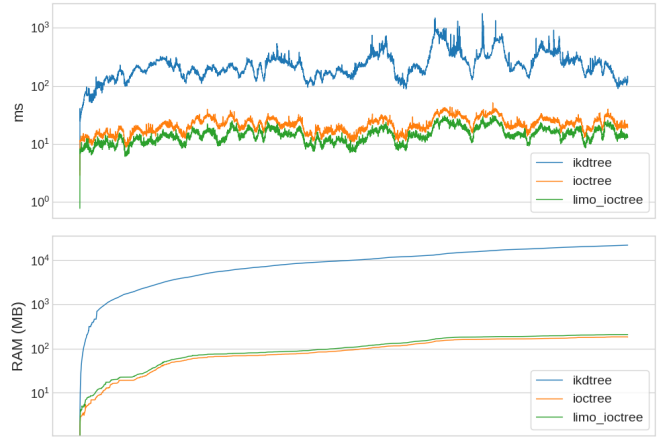


Fig. 4. Per-frame computation time on the ntu_day_01 sequence in a simulation setup where three IESKF iterations are executed for every LiDAR frame. Under these conditions, the octree-based methods sustain real-time performance, whereas ikd-Tree exhibits substantially higher and more variable processing times.

drift. LIMOncello, in contrast, maintains a stable trajectory throughout the tunnel.

In feature-rich environments and well-conditioned trajectories, LIMOncello achieves accuracy comparable to state-of-the-art methods such as RESPLE and FAST-LIO2. While continuous-time splines can better model smooth motion in these cases, LIMOncello provides a viable alternative with improved robustness.

The proposed i-Octree mapping backend further supports practical deployment by sustaining real-time performance, maintaining stable memory usage, and achieving lower runtime than both the baseline i-Octree and ikd-Tree.

VI. CONCLUSION

LIMOncello demonstrates that a discrete-time SGal(3)-based formulation can deliver strong robustness in challenging operating conditions while maintaining state-of-the-art accuracy. By providing a better motion propagation, the proposed approach enables reliable operation in geometrically degenerate environments.

The City02 experiment highlights LIMOncello’s robustness in severely feature-degenerate conditions, whereas alternative state-of-the-art approaches diverge under the same settings. Across feature-rich environments, LIMOncello remains comparable to existing methods while offering a simpler and more stable state representation. Combined with a real-time i-Octree mapping backend, the system achieves a favorable balance between robustness, accuracy, and efficiency.

APPENDIX

S^2 manifold, \oplus - \ominus parameterization and Jacobians

Following [4], the \oplus and \ominus operators are defined in terms of a local tangent basis $\mathbf{B}(\mathbf{x}) \in \mathbb{R}^{3 \times 2}$, whose columns span the tangent plane at \mathbf{x} . Specifically, for a point $\mathbf{x} \in S^2$ and a

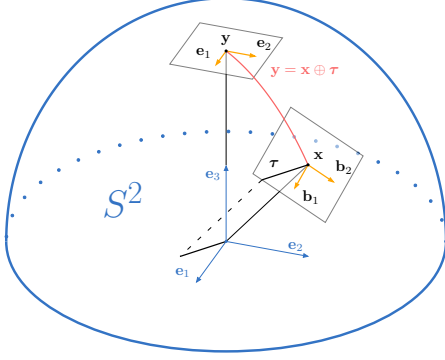


Fig. 5. Geometric interpretation of the \oplus operation on S^2 . The tangent basis $[\mathbf{b}_1, \mathbf{b}_2]$ at \mathbf{x} spans the plane $T_{\mathbf{x}}S^2$, where the increment $\boldsymbol{\tau}$ is defined. The updated point $\mathbf{y} = \mathbf{x} \oplus \boldsymbol{\tau}$ is obtained by mapping $\boldsymbol{\tau}$ to a 3-dimensional tangent vector via $\mathbf{B}(\mathbf{x})$ and rotating \mathbf{x} by this vector, interpreted as an angle-axis rotation.

tangent increment $\boldsymbol{\tau} \in \mathbb{R}^2$, the \oplus and \ominus operations are given by

$$\mathbf{x} \oplus \boldsymbol{\tau} = \text{SO}(3) \text{Exp}(\mathbf{B}(\mathbf{x}) \boldsymbol{\tau}) \mathbf{x}, \quad (21a)$$

$$\mathbf{y} \ominus \mathbf{x} = \mathbf{B}(\mathbf{x})^\top \left(\theta \frac{\mathbf{x} \times \mathbf{y}}{\|\mathbf{x} \times \mathbf{y}\|} \right), \quad \theta = \text{atan2}(\|\mathbf{x} \times \mathbf{y}\|, \mathbf{x}^\top \mathbf{y}), \quad (21b)$$

where $\mathbf{B}(\mathbf{x}) = [\mathbf{b}_1 \ \mathbf{b}_2] \in \mathbb{R}^{3 \times 2}$ contains two orthonormal basis vectors spanning the tangent plane at \mathbf{x} .

To construct $\mathbf{B}(\mathbf{x})$, we follow [4] and define a rotation that maps the canonical basis onto a frame whose third axis aligns with \mathbf{x} . Using the reference axis \mathbf{e}_3 , let

$$\mathbf{R}(\mathbf{x}) = \text{SO}(3) \text{Exp} \left(\frac{\mathbf{e}_3 \times \mathbf{x}}{\|\mathbf{e}_3 \times \mathbf{x}\|} \text{atan2}(\|\mathbf{e}_3 \times \mathbf{x}\|, \mathbf{e}_3^\top \mathbf{x}) \right), \quad (22a)$$

$$\mathbf{B}(\mathbf{x}) = \mathbf{R}(\mathbf{x}) [\mathbf{e}_1 \ \mathbf{e}_2]. \quad (22b)$$

With this choice, increments $\boldsymbol{\tau}$ live in \mathbb{R}^2 as illustrated in Fig. 5. Closed-form Jacobians are given in [4, eq. (69), (70)].

However, when $\theta \rightarrow 0$, a first-order Taylor approximation is applied to atan2 , and (21b) simplifies to $\mathbf{y} \ominus \mathbf{x} \simeq \mathbf{B}(\mathbf{x})^\top (\mathbf{x} \times \mathbf{y})$. Therefore,

$$\frac{\partial(\mathbf{y} \ominus \mathbf{x})}{\partial \mathbf{y}} \simeq \mathbf{B}(\mathbf{x})^\top [\mathbf{x}]_{\times}. \quad (23)$$

Conversely, when $\theta \rightarrow \pi$, there exist infinitely many tangent vectors that rotate \mathbf{x} into \mathbf{y} . Following the convention in [4], we choose

$$\mathbf{y} \ominus \mathbf{x} = \begin{bmatrix} \pi \\ 0 \end{bmatrix}. \quad (24)$$

REFERENCES

- [1] W. Xu and F. Zhang, “Fast-lio: A fast, robust lidar-inertial odometry package by tightly-coupled iterated kalman filter,” *IEEE Robotics and Automation Letters*, vol. 6, no. 2, pp. 3317–3324, 2021.
- [2] W. Xu, Y. Cai, D. He, J. Lin, and F. Zhang, “Fast-lio2: Fast direct lidar-inertial odometry,” *IEEE Transactions on Robotics*, vol. 38, no. 4, pp. 2053–2073, 2022.
- [3] C. Bai, T. Xiao, Y. Chen, H. Wang, F. Zhang, and X. Gao, “Faster-lio: Lightweight tightly coupled lidar-inertial odometry using parallel sparse incremental voxels,” *IEEE Robotics and Automation Letters*, vol. 7, no. 2, pp. 4861–4868, 2022.
- [4] D. He, W. Xu, and F. Zhang, “Symbolic representation and toolkit development of iterated error-state extended kalman filters on manifolds,” *IEEE Transactions on Industrial Electronics*, vol. 70, no. 12, pp. 12 533–12 544, 2023.
- [5] Y. Cai, W. Xu, and F. Zhang, “ikd-tree: An incremental kd-tree for robotic applications,” 2021. [Online]. Available: <https://arxiv.org/abs/2102.10808>
- [6] C. Wu, Y. You, Y. Yuan, X. Kong, Y. Zhang, Q. Li, and K. Zhao, “Voxelmap++: Mergeable voxel mapping method for online lidar-inertial odometry,” *IEEE Robotics and Automation Letters*, vol. 9, no. 1, pp. 427–434, 2024.
- [7] X. Yang, W. Li, Q. Ge, L. Suo, W. Tang, Z. Wei, L. Huang, and B. Wang, “C3p-voxelmap: Compact, cumulative and coalescible probabilistic voxel mapping,” in *2024 IEEE/RSJ International Conference on Intelligent Robots and Systems (IROS)*, 2024, pp. 7908–7915.
- [8] K. Chen, R. Nemirow, and B. T. Lopez, “Direct lidar-inertial odometry: Lightweight lio with continuous-time motion correction,” in *2023 IEEE International Conference on Robotics and Automation (ICRA)*, 2023, pp. 3983–3989.
- [9] Z. Cao, W. Talbot, and K. Li, “Resple: Recursive spline estimation for lidar-based odometry,” *IEEE Robotics and Automation Letters*, vol. 10, no. 10, pp. 10 666–10 673, 2025.
- [10] J. Solà, J. Deray, and D. Atchuthan, “A micro lie theory for state estimation in robotics,” 2021. [Online]. Available: <https://arxiv.org/abs/1812.01537>
- [11] A. Barrau and S. Bonnabel, “The invariant extended kalman filter as a stable observer,” *IEEE Transactions on Automatic Control*, vol. 62, no. 4, pp. 1797–1812, 2017.
- [12] C. Zhang, J. Zhang, Q. Liu, Y. Liu, and J. Qin, “Si-lio: High-precision tightly-coupled lidar-inertial odometry via single-iteration invariant extended kalman filter,” *IEEE Robotics and Automation Letters*, vol. 10, no. 1, pp. 564–571, 2025.
- [13] G. Delama, A. Fornasier, R. Mahony, and S. Weiss, “Equivariant imu preintegration with biases: A galilean group approach,” *IEEE Robotics and Automation Letters*, vol. 10, no. 1, pp. 724–731, 2025.
- [14] J. Zhu, H. Li, Z. Wang, S. Wang, and T. Zhang, “i-octree: A fast, lightweight, and dynamic octree for proximity search,” in *2024 IEEE International Conference on Robotics and Automation (ICRA)*, 2024, pp. 12 290–12 296.
- [15] J. Deray and J. Solà, “manif.” [Online]. Available: <https://www.theoj.org/joss-papers/joss.01371/10.21105.joss.01371.pdf>
- [16] J. Solà, “Quaternion kinematics for the error-state kalman filter,” 2017. [Online]. Available: <https://arxiv.org/abs/1711.02508>
- [17] R. Mahony, J. Kelly, and S. Weiss, “Galilean symmetry in robotics,” 2025. [Online]. Available: <https://arxiv.org/abs/2510.10468>
- [18] J. Kelly, “Making space for time: The special galilean group and its application to some robotics problems,” 2024. [Online]. Available: <https://arxiv.org/abs/2409.14276>
- [19] M. Fourmy, D. Atchuthan, N. Mansard, J. Solà, and T. Flayols, “Absolute humanoid localization and mapping based on imu lie group and fiducial markers,” in *2019 IEEE-RAS 19th International Conference on Humanoid Robots (Humanoids)*, 2019, pp. 237–243.
- [20] J. Kelly, “All about the galilean group $\text{sgal}(3)$,” 2025. [Online]. Available: <https://arxiv.org/abs/2312.07555>
- [21] T.-M. Nguyen, S. Yuan, T. H. Nguyen, P. Yin, H. Cao, L. Xie, M. Wozniak, P. Jensfelt, M. Thiel, J. Ziegenbein, and N. Blunder, “Mcd: Diverse large-scale multi-campus dataset for robot perception,” in *2024 IEEE/CVF Conference on Computer Vision and Pattern Recognition (CVPR)*, 2024, pp. 22 304–22 313.
- [22] J. Frey, T. Tuna, L. F. T. Fu, C. Weibel, K. Patterson, B. Krummenacher, M. Müller, J. Nubert, M. Fallon, C. Cadena, and M. Hutter, “Boxi: Design decisions in the context of algorithmic performance for robotics,” 2025. [Online]. Available: <https://arxiv.org/abs/2504.18500>
- [23] M. Jung, S. Jung, and A. Kim, “Asynchronous multiple lidar-inertial odometry using point-wise inter-lidar uncertainty propagation,” *IEEE Robotics and Automation Letters*, vol. 8, no. 7, pp. 4211–4218, 2023.
- [24] M. Grupp, “evo: Python package for the evaluation of odometry and slam.” <https://github.com/MichaelGrupp/evo>, 2017.